

Cerebral cortical hypoplasia with abnormal morphology of pyramidal neuron in growth-retarded mouse (*grt/grt*)

Miwa Horiuchi-Hirose¹, Shigeyoshi Saito^{2,3}, Chika Sato⁴, Junya Aoyama⁴, Tetsuya Kobayashi⁴, and Kazuhiko Sawada^{1,*}

¹Department of Nutrition, Faculty of Medical and Health Sciences, Tsukuba International University, Tsuchiura, Ibaraki, Japan, *Email: k-sawada@tius.ac.jp; ²Department of Medical Engineering, Division of Health Sciences, Osaka University Graduate School of Medicine, Suita, Osaka, Japan; ³Center for Information and Neural Networks (CiNet), National Institute of Information and Communications Technology, Osaka University, Suita, Osaka, Japan; ⁴Division of Life Science, Graduate School of Science and Engineering, Saitama University, Saitama, Japan

The purpose of this study was to quantitatively characterize structural abnormalities of the cerebrum in a growth-retarded mouse (*grt/grt*) with a tyrosylprotein sulfotransferase 2 gene defect. Three-dimensional computed tomography (CT) images were obtained from fixed brains of male homogenous *grt/grt* ($n=5$) and heterozygous *grt/+* ($n=5$) mice at 15 weeks of age, and volumes of representative cerebral regions were calculated on the basis of those images. Following CT measurements, cryosections of the brain were made, and immunohistochemistry for NeuN and SMI-32 was carried out. By CT-based volumetry, region-specific reductions in volumes were marked in the cerebral cortex and white matter, but not in other cerebral regions of *grt/grt*. When quantitatively evaluating the shape of the cerebral cortex, the frontooccipital length of the cortex was significantly smaller in *grt/grt* than in *grt/+*, whereas the cortical width was not altered in *grt/grt*. On the other hand, both cortical thickness and density of NeuN-immunopositive neurons in three distinctive cortical regions, i.e., the primary motor cortex, barrel field of primary somatosensory cortex and primary visual cortex, were not different between *grt/grt* and *grt/+*. By semi-quantitative immunohistochemical analysis, the intensity of SMI-32 immunostaining was significantly weaker in *grt/grt* than in *grt/+* in the three cortical areas examined. SMI-32 staining was reduced, particularly in layer III pyramidal neurons in *grt/grt*, while it was sustained in multipolar neurons. The present results suggest that cerebral abnormalities in *grt/grt* mice are characterized by cortical hypoplasia at the frontooccipital axis with immature pyramidal neurons and insufficient development of callosal fibers.

Key words: growth-retarded mouse, pyramidal neuron, cerebral cortex, volumetry, hypothyroidism, tyrosylprotein sulfotransferase 2

ABBREVIATIONS:

A – auditory cortex
Amg – amygdala
Cb – cerebellum
cc – corpus callosum
Cg – cingulate cortex
CPu – caudate putamen
DCN – deep cerebellar nucleus
Dien – diencephalon

ec – external capsule
FrA – frontal association cortex
gcc – genu of corpus callosum
Hip – hippocampus
Hyp – hypothalamus
I – insular cortex
LV – lateral ventricle
M1 – primary motor cortex
M2 – secondary motor cortex
Mb – midbrain
Ob – olfactory bulb
ot – optic tract
pc – posterior commissure
Pt – parietal association cortex

Correspondence should be addressed to K. Sawada
Email: k-sawada@tius.ac.jp

Received 20 December 2013, accepted 26 May 2014

RS – retrosplenial agranular cortex
 S1 – primary somatosensory cortex
 S1BF – barrel field of primary somatosensory cortex
 S2 – secondary somatosensory cortex
 scc – splenium of corpus callosum
 Th – thalamus
 V1 – primary visual cortex
 V2 – secondary visual cortex
 WM – cerebral white matter

INTRODUCTION

Growth-retarded mouse (*grt*) is a spontaneous mutant, arisen by a sister × brother mating of phenotypically normal Snell's dwarf (DW/J strain) mice (Yoshida et al. 1994). This mouse carries a recessive missense mutant allele on chromosome 5 (Agui et al. 1997) that encodes a gene for tyrosylprotein sulfotransferase 2 (Tpst2) (Sasaki et al. 2007). Since Tpst2 is crucial for thyroid-stimulating hormone (TSH) signaling by the tyrosine sulfation of TSH receptors (Costagliola et al. 2002), homozygous *grt/grt* mice show hypothyroid characteristics by TSH receptor insensitivity (Kobayashi et al. 2001, Sasaki et al. 2007) such as an elevation of serum/plasma TSH levels (Kobayashi et al. 2001, Sasaki et al. 2007), but they have a reduction in serum/plasma thyroxine (T_4) levels (Yoshida et al. 1994, Kobayashi et al. 2001), and a characteristic pause of growth with the delay of pubertal growth onset (Yoshida et al. 1994).

Volumetric analysis is a quantitative approach using imaging techniques such as magnetic resonance imaging (MRI) and computed tomography (CT), allowing a comparison of absolute volumes of brain structures between two or more groups, or time-dependent changes. There have been a number of studies attempting MRI brain volumetry in human neurodevelopmental disorders such as schizophrenia (Howard et al. 1994, Joyal et al. 2004, Whitworth et al. 2005, Molina et al. 2006, Saze et al. 2007, Sun et al. 2009, Verma et al. 2009, Preuss et al. 2010, Iwashiro et al. 2012) and autism (Zeegers et al. 2009, Bigler et al. 2010). However, volumetric studies regarding the brain's structural changes in small laboratory animal models such as mice and rats are limited in number (Sawiak et al. 2009, Acosta et al. 2010, Scheenstra et al. 2011, Heikkinen et al. 2012, Sawada et al. 2013). The present study aimed to quantitatively characterize cerebral structural abnormalities in a homozygous *grt/grt*

mouse by CT-based volumetry and semi-quantitative immunohistochemistry using markers for specific populations of cerebral cortical neurons.

METHODS

Animals

Male growth-retarded mice (*grt/grt*), raised on a DW/J background, were obtained by intercrossing normal phenotype (+/+ or *grt*+) females with *grt/grt* males. Male littermate heterozygous mice (*grt*+) were used as controls¹. Mice were given a pellet diet (MR Breeder, Labo Nosan, Yokohama, Japan) and tap water *ad libitum*, and were kept at 23±1°C with 50±10% relative humidity under 12-h artificial illumination at the animal facility of Saitama University.

Male *grt/grt* mice ($n=5$; body weight, 17.4±1.9 g) and male *grt*+/ mice ($n=5$; body weight, 28.9±1.0 g) at 15 weeks of age were deeply anesthetized with an intraperitoneal injection of sodium pentobarbital (0.63 mg/10 g body weight), and were perfused with 0.9% NaCl followed by 4% paraformaldehyde in 0.1 M phosphate buffer, pH 7.4 (PFA solution). Brains were removed from skulls, and immersed in the same fixative before use.

Micro-CT procedure

Preceding micro-CT evaluation, brain samples were soaked in 150 mg/ml nonionic iodinated contrast agent (Iopamiron, Bayer Schering Pharma, Japan) in 7.5% PFA solution at 4°C for 14 days. Computed tomography images were acquired using three-dimensional (3D) micro-CT (RmCT, Rigaku Co., Tokyo, Japan) with a resolution of 39×39×39 μm^3 , a tube voltage peak of 90 kV peak, and a tube current of 200 μA with a scan time of 8 minutes. The cathode was made of tungsten (effective focal spot size =5 μm). The images of the object were reconstructed using a Feldkamp algorithm. Tomographic images were obtained using 3D

¹ As mentioned in the Introduction, homozygous *grt/grt* mice show hypothyroid characteristics by TSH receptor insensitivity and a characteristic pause of growth with the delay of pubertal growth onset as striking mutant phenotypes. The mean body weight does not differ between *grt*+/ and wild-type +/+ mice at 5 weeks of ages (Sasaki et al. 2007), while phenotypically normal mice (+/+ or *grt*+/) significantly marked greater body weight than *grt/grt* mice during 12 to 24 weeks of age (Yoshida et al. 1994). Regarding TSH receptor insensitivity, there are no differences in TSH-induced T_3 and T_4 releases and cAMP production in thyroid glands between *grt*+/ and +/+ mice during 12 to 24 weeks of age (Kobayashi et al. 2001). Thus, *grt*+/ mice have endocrine and growth characteristics equivalent to +/+ mice, and it is not considered a problem to use *grt*+/ mice as controls.

imaging software (i-VIEW, Morita Co., Tokyo, Japan). *Ex vivo* micro-CT shows inverted images to better clarify the white and gray matter structures (Saito and Murase 2012).

3D volume-rendered images and volumetric analysis

All CT images were used for the 3D reconstruction and quantitative measurements. Cerebral regions, i.e., the cerebral cortex, caudate putamen, amygdalae, hippocampus, olfactory bulb, and cerebral white matter (including corpus callosum, internal capsule, external capsule anterior commissure, and fornix), were semi-automatically segmented on CT images using the “Morpho” tool of SliceOmatic software v. 4.3 (TomoVision, Montreal, Canada) based on image contrast as well as the user’s knowledge of the anatomy. Other cerebral regions listed above were also segmented. Boundaries of each region were determined in reference with the procedure of Dorr and coauthors (2008). Segmented images were then analyzed using the 3D-rendering module of the same software. The cerebral image was rendered in 3D using the surface projection algorithm which best visualized the surface of the cerebrum. 3D-rendered images were then rotated and manipulated in a manner that best visualized brain morphology by a linear registration method using SliceOmatic software. The terminology used was based on the Atlas of Paxinos and Franklin (2004).

The volumetric analysis procedure was performed as in our previous studies (Sawada et al. 2013). Segmented areas of each brain region were measured using SliceOmatic software. The volumes were calculated by multiplying the combined areas by the slice thickness (39 μm), with the total volume of segmented regions being regarded as the cerebral volume.

Frontooccipital length, width and surface area of cerebral cortex

The frontooccipital length from the frontal pole to the occipital pole of the cerebral cortex was measured on 3D-rendered images using SliceOmatic software. Widths of the cerebral cortex were also measured at the anterior commissure and posterior commissure on the 3D-rendered images using the same software. The surface area of the cerebral cortex was computed from measurements obtained by a semiautomatic delineation

of the most superficial region of the cortex (cortical perimeter) on coronal CT images using SliceOmatic software.

Histology and immunohistochemistry

Following CT measurements, the brains were cryoprotected by immersion in 30% sucrose in 10 mM phosphate-buffered saline (PBS) overnight. They were frozen in Optimal Cutting Temperature embedding compound, and sectioned serially in the coronal plane at 40 μm by a Retratome (REM-700; Yamato Koki Industrial, Asaka, Japan) with a refrigeration unit (Electro Freeze MC-802A, Yamato Koki Industrial Co., Ltd.). Some sections were Nissl-stained as an anatomical reference to CT images.

All immunohistochemical procedures were performed on floating sections. The sections were treated with Antigen Retrieval Reagent UNIVERSAL (R&D Systems, Minneapolis, MN) for 30 min in a 90°C water bath, and then cooled for 30 min at 4°C. After washing with PBS, sections were reacted with a mouse anti-SMI-32 monoclonal antibody (1:1000; Covance, Princeton, NJ, USA), or a rabbit anti-NeuN polyclonal antibody (1:1000; Millipore, Billerica, CA, USA), containing 10% normal goat serum at 4°C overnight. Anti-SMI-32 and anti-NeuN recognized non-phosphorylated forms of the neurofilament heavy chain, and the DNA-binding, neuron-specific protein, respectively. Those two antibodies produced highly-specific immunostaining in the mouse brain (Van der Gucht et al. 2007, Bath et al. 2012). After incubation, the sections were rinsed with PBS and reacted with biotinylated anti-mouse IgG or biotinylated anti-rabbit IgG. The immunoreactive products were visualized by a Vectastain ABC elite kit (Vector Labs., Inc., Burlingame, CA) using 0.01% 3,3'-diaminobenzidine tetrachloride (DAB) (Sigma) in 0.03% H_2O_2 as a chromogen. To enable a comparison of SMI-32 and NeuN immunostaining, all sections were processed in identical staining conditions. The same set of solutions were used for the respective times and temperatures of incubations for the antigen retrieval treatment; the primary and secondary antibodies and the DAB color development; and the time, temperature and number of PBS washings. Evaluation of the intensity of SMI-32 immunostaining in the cortex was performed using a modified protocol designed for our previous study (Sawada et al. 2008). Images of immunostained sections were acquired with a microscope using a $\times 4$ objective

(Axio Imager A1; Zeiss, Göttingen, Germany). The immunostaining intensity was evaluated by its optical density (OD) on captured images by using ImageJ software (National Institutes of Health, Bethesda, USA). Captured images of three distinct cortical areas, i.e., the primary motor cortex (M1), barrel field of primary somatosensory cortex (S1BF) and primary visual cortex (V1), which were defined in the SMI-32 immunostained sections with reference to the Atlas of Paxinos and Franklin (2004), were converted into a grayscale digital image. The brightness of each pixel ranged from 0 to 255 gray levels. The threshold of the OD value of each section was determined by averaging five random polygons (area of POLYGON = $150 \mu\text{m}^2$) of the unstained neuropil. The OD within a rectangular frame at a width of $200 \mu\text{m}$ and a length covering the entire depth of the cortex was measured in each cortical area as the SMI-32 immunostaining intensity using ImageJ software. The mean of five points more than $30 \mu\text{m}$ apart was used for each animal when measuring the OD.

The number of neurons in the cortical layers I, II/III, IV, V and VI, was evaluated on captured images of NeuN-immunostained sections of the M1, S1BF and V1. Captured images were converted to black and white. The threshold of the OD value of each section was determined as the background staining by averaging five random polygons (area of POLYGON = $150 \mu\text{m}^2$) of the unstained neuropil. Then, the background staining was removed from the captured images. Black particles greater than $5 \mu\text{m}$ in a minor axis were defined as NeuN-immunopositive neurons, and were counted within a rectangular frame with a width of $200 \mu\text{m}$ and a length covering each cortical layer, using “Particle analyze” tool of ImageJ software. The mean of five points more than $30 \mu\text{m}$ apart was used for each animal when counting the number of neurons.

Cortical thickness

Thickness of the entire depth of the cerebral cortex was measured on both coronal CT images and captured images of Nissl-stained sections using ImageJ software (National Institutes of Health, Bethesda, USA). Using a modified protocol originally designed in our previous study (Horiuchi-Hirose et al. 2012), thickness of the cortical layers I, II/III, IV, V and VI were further measured on captured images of NeuN-immunostained sections. Measurements were obtained in three distinct cortical areas; the M1, S1BF and V1 in reference to the Atlas of Paxinos and Franklin (2004).

We further mapped the average thickness of the cortex, coded in color on the 3D surface of the cerebrum. The 3D color maps of cortical thickness were obtained from computing the distance along the vertex normal to the normal's intersection with the closest triangle in each vertex on segmented cortical surface (Zhang et al. 2003, Huang et al. 2009), by using Amira ver 5.2 (Visage Imaging, Inc., San Diego, CA, USA). The known cortical areas of the mouse cerebrum (modified from Paxinos and Franklin 2004) were overlayed on 3D color maps of the cortical thickness using “3D annotation” tool of Amira software in reference with coronal CT images by “OrthoSlice” tool of the same software.

Thickness of corpus callosum

Thickness of corpus callosum was measured on coronal CT images. Both measurements were conducted at the midline of coronal images around the center of the anterior commissure. The mean of five points from five serial images was used for each animal when measuring thickness.

Statistics

Data on bar graphs of each figure were represented as mean \pm SD. Significant differences in cerebral volume, the total area of the cerebral cortical surface, the frontooccipital length, and the thickness of corpus callosum were evaluated statistically by one-way ANOVA, followed by a two-tailed Student's *t*-test.

Mutant-related changes in volumes of each brain region were statistically evaluated by two-way ANOVA using genotypes (*grt/grt* and *grt/+*) and the brain regions as factors. Mutant-related changes in the intensity of SMI-32 immunostaining in the cortex were also evaluated by two-way ANOVA using genotypes (*grt/grt* and *grt/+*) and the cortical areas (M1, S1BF and V1) as factors. Furthermore, mutant- and cortical region-related changes in both thickness and the number of neurons in each cortical layer were statistically analyzed by two-way ANOVA using genotypes and cortical layers (layers I, II/III, IV, V and VI) as factors. Scheffe's test was used as *post-hoc* testing to compare *grt/grt* and *grt/+* mice.

Ethics

Experimental procedures in the present study were conducted in accordance with the guidelines of the

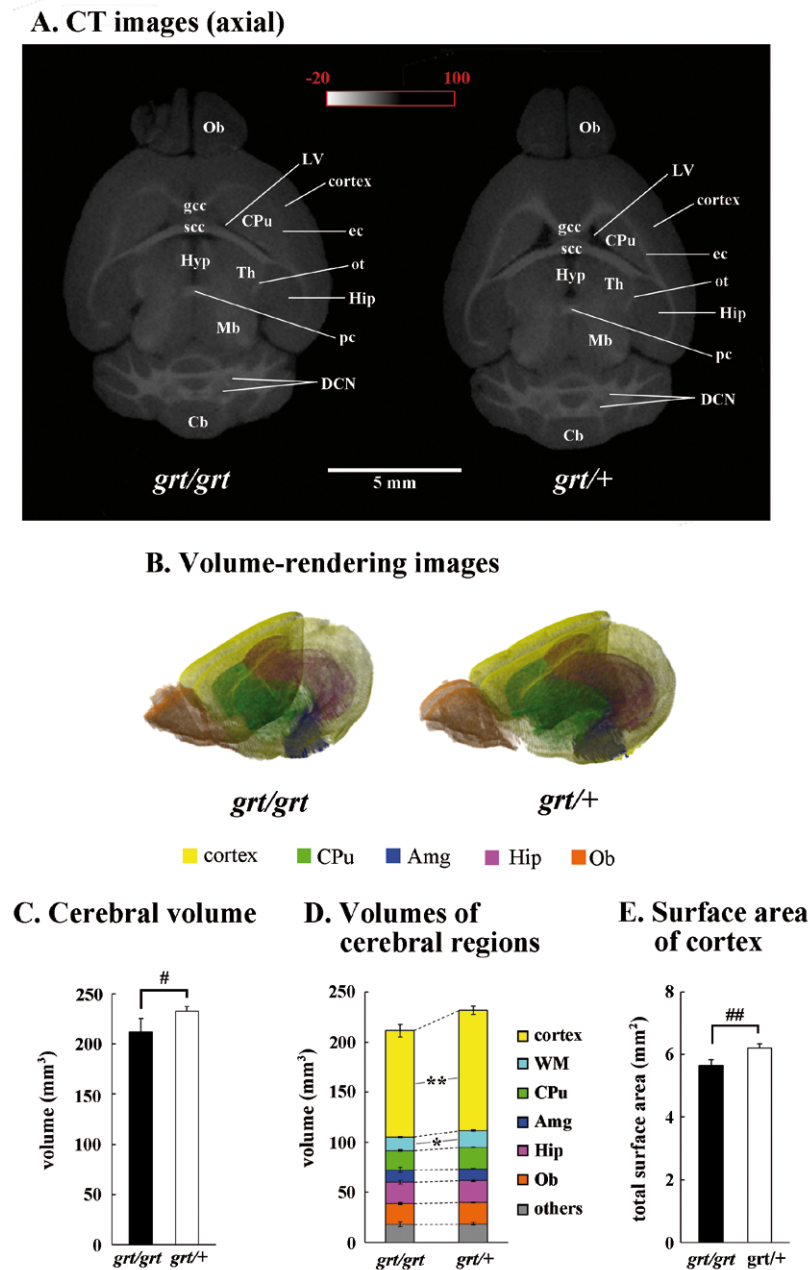


Fig. 1. Representative axial CT images and volume-rendered images of cerebrum, and volumes of cerebral structures. (A) Axial CT images of the brain of *grt/grt* (left) and *grt/+* (right) mouse. While the brain was slightly smaller in *grt/grt* than in *grt/+*, the structural organization and histoarchitecture of cerebrum were sustained in *grt/grt*. The range of Hounsfield units used in CT images is shown enclosed by a red frame. (B) Three-dimensional volume-rendered images of *grt/grt* (left) and *grt/+* (right). The following cerebral structures were reconstructed: cortex (yellow); caudate putamen (CPu, light green); amygdala (Amg, blue); hippocampus (Hip, purple); and olfactory bulb (Ob, orange). The brainstem and cerebellum were not included in the rendered images. (C) Bar graphs of volume of cerebrum. $^{\#}P < 0.05$ (Student's *t*-test). (D) Stacked bar graphs of cerebral region volumes. Two-way ANOVA revealed significant effects on genotypes ($F_{6,56} = 1908.712$; $P < 0.001$), cerebral regions ($F_{1,56} = 21.513$; $P < 0.001$), and their interaction ($F_{6,56} = 9.274$; $P < 0.001$). $^{\ast}P < 0.05$; $^{\ast\ast}P < 0.001$ (Scheffe's test). (E) Bar graph of total surface area of cerebral cortex, $^{\ast}P < 0.05$ (Student's *t*-test). (Amg) amygdala; (Cb) cerebellum; (CPu) caudate putamen; (DCN) deep cerebellar nucleus; (ec) external capsule; (gcc) genu of corpus callosum; (Hip) hippocampus; (Hyp) hypothalamus; (LV) lateral ventricle; (Mb) midbrain; (Ob) olfactory bulb; (ot) optic tract; (pc) posterior commissure; (scc) splenium of corpus callosum; (Th) thalamus; (WM) cerebral white matter.

National Institutes of Health (NIH) for the Care and Use of Laboratory Animals. The Institutional Animal Care and Use Committee of Saitama University approved the procedures, and all efforts were made to minimize the number of animals used and their suffering.

RESULTS

CT Images

Representative axial CT images of the brains of *grt/grt* and *grt/+* were shown in Figure 1A. CT images could distinguish gray and white matter structures by their contrast, and cerebral regions, i.e., the cerebral cortex, caudate putamen, amygdala, and hippocampus were distinguishable as gray matter structures. As for white matter structures, the corpus callosum, external capsule, posterior commissure and optic tract could be seen on the axial images shown in Figure 1A. There was no obvious difference in the structural organization of the brain between *grt/grt* or *grt/+*. However, *grt/grt* had a relatively round-shaped brain with thinner white matter structures when compared to *grt/+*.

3D reconstruction and quantitative analyses

In order to detect morphological anomalies in the *grt* cerebrum, 3D morphology, topology and volumes of major structures of cerebral gray and white matter were examined in *grt/grt* mice, and compared to heterozygous *grt/+* controls. 3D volume-rendered images of the brain were calculated using CT images. There were no obvious differences in the 3D morphology and topology of major gray matter structures of the cerebrum, i.e., the caudate putamens, amygdala, hippocampus and olfactory bulb between *grt/grt* and *grt/+* (Fig. 1B). Cerebral volume was calculated based on CT images. A significantly lower brain volume of the cerebrum was detected in *grt/grt* ($P<0.05$) (Fig. 1C). In order to specify whether volume reduction of the *grt/grt* cerebrum was overall or region-specific, we calculated volumes of the cerebral regions, i.e., the caudate putamen, amygdala, hippocampus, olfactory bulb, cerebral white matter, and others. Two-way ANOVA revealed significant effects on genotypes ($F_{6,56}=1908.712$; $P<0.001$), cerebral regions ($F_{1,56}=21.513$; $P<0.001$), and their interaction ($F_{6,56}=9.274$; $P<0.001$). Significantly-reduced volumes of the cortex ($P<0.001$) and white matter ($P<0.05$) in *grt/grt* rather than in *grt/+* were

detected by *post-hoc* testing. Such differences were clearly shown by the stacked bar graph of the volume of all cerebral regions (Fig. 1D). As well as cortical volume, total surface area of the cortex was significantly lower in *grt/grt* mice than that in *grt/+* ($P<0.001$) (Fig. 1E). Thus, region-specific volume reductions in the cerebral cortex and white matter were attributed to the decreased size of cerebrum in *grt/grt* mice.

In order to evaluate the shape of the cerebral cortex quantitatively, the frontooccipital length and the width of the cerebral cortex were measured using volume-rendered images. The frontooccipital length was smaller in *grt/grt* than in *grt/+* ($P<0.001$) (Fig. 2A). However, there were no differences in cortical widths, either at the anterior commissure or posterior commissure, between two *grt/grt* and *grt/+* (Fig. 2B). Thus, the relatively round-shaped brain in *grt/grt* mice was involved in reducing the volume of the cerebral cortex at the rostrocaudal axis.

Cortical thickness

In order to clarify whether the reduced volume of the *grt* cortex can be attributed to changes in the thickness of specific cortical regions, cortical thickness was examined using coronal CT images and Nissl-stained coronal sections. Since the neuronal density in the six cortical layers and the arrangement of SMI-32-immunopositive pyramidal neurons in the neocortex were to be further examined in the next section, measurements of cortical thickness were performed in cortical areas that were comparable to the results

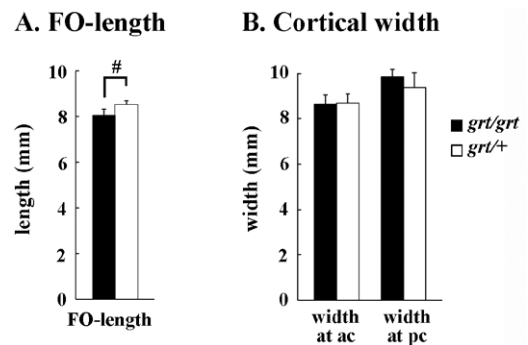


Fig. 2. Frontooccipital length and width of cerebral cortex. (A) Frontooccipital length (FO-length) of the cortex. $^{\#}P<0.05$ (Student's *t*-test). (B) Width of cortex at anterior commissure (ac) and posterior commissure (pc). There were no differences in width at either region between *grt/grt* and *grt/+*.

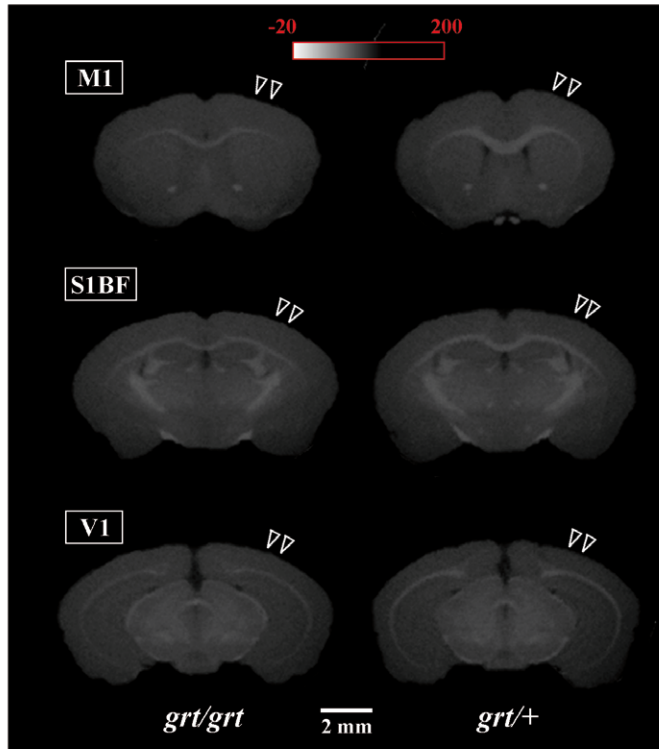
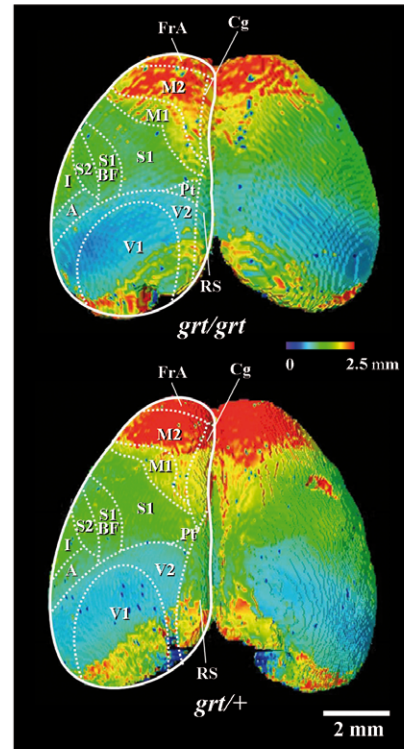
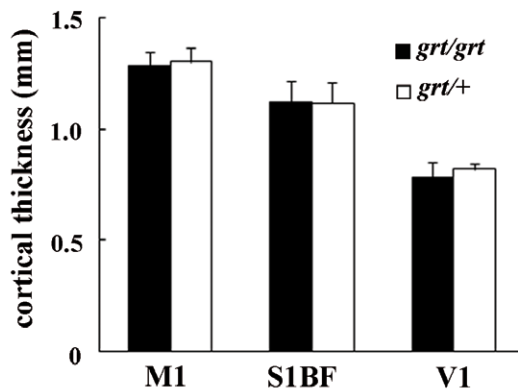
A. Coronal CT images of three cortical areas**C. 3D color maps****B. Cortical thickness**

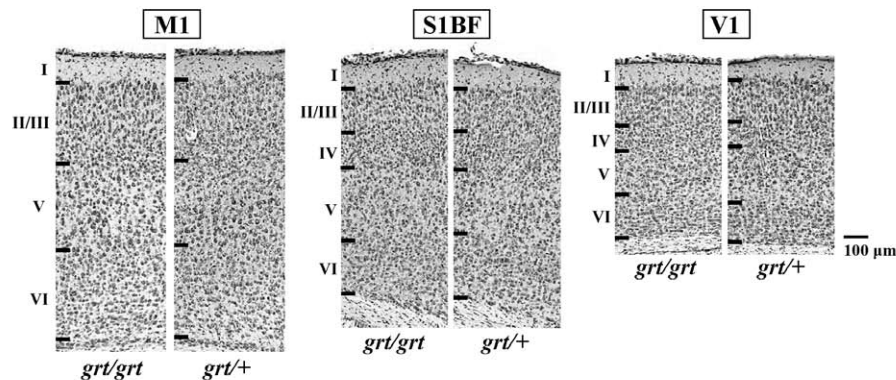
Fig. 3. Cortical thickness obtained from CT images. (A) Coronal CT images of three cortical areas. Arrowheads indicate the primary motor cortex (M1), barrel field of primary somatosensory cortex (S1BF) and primary visual cortex (V1). Measurements were conducted in those regions. The range of Hounsfield units used for CT images is shown enclosed in a red frame. (B) Measurements of cortical thickness of M1, S1BF and V1 obtained from coronal CT images. There was no difference in cortical thickness between *grt/grt* and *grt/+* in three cortical areas examined. (C) Three-dimensional (3D) color maps of cortical thickness obtained from computation on segmented cortical surface. The known cortical areas of mouse cerebrum, which was reconstructed in 3D in reference with coronal image illustrations of the Atlas of Paxinos and Franklin (2004), were overlaid on 3D color maps of cortical thickness. Cortical thickness varied among functional cortical areas, and boundaries of each cortical area were clearly defined on 3D color maps of cortical thickness. (A) auditory cortex; (Cg) cingulate cortex; (FrA) frontal association cortex; (I) insular cortex; (M2) secondary motor cortex; (Pt) parietal association cortex; (RS) retrosplenial agranular cortex; (S1) primary somatosensory cortex; (S2) secondary somatosensory cortex; (V2) secondary visual cortex.

obtained from coronal CT images and coronal histological sections. We selected three areas that had different functions and were located vertically to pia surfaces on coronal images, i.e., the primary motor cortex (M1), barrel field of primary somatosensory cortex (S1BF) and primary visual cortex (V1).

Figure 3A shows three regions where cortical thickness was measured on representative coronal CT images. A region-related difference in cortical thickness was revealed by two-way ANOVA ($F_{2,24}=336.6968$, $P<0.001$), while the thickness of each cortical area did not differ between the two genotypes of mice (Fig. 3B). Three-dimensional color maps of cortical thicknesses were obtained from computation of the segmented cortical surface (Fig. 3C). The maps revealed a regional difference in cortical thickness through the cerebral cortex, characterized by reducing of thickness in a rostrocaudal gradient manner. The known cortical areas of the mouse cerebrum (modified from Paxinos

and Franklin 2004) were overlaid on the 3D color maps of cortical thickness. As shown in Figure 3C, the distribution pattern of cortical thickness was reminiscent of the known cortical areas. For example, the thickest rostral region (indicated by red) corresponded to the frontal association (FrA) and secondary motor (M2) cortices; its adjacent region (indicated by yellow) corresponded to the M1; moderate thickness in the parietotemporal region (indicated by green) corresponded to the primary (S1 and S1BF) and secondary (S2) somatosensory cortices; and the thinnest caudal region (indicated by light blue and blue) corresponded to the auditory cortex (A) and the primary (V1) and secondary (V2) visual cortices. Thicknesses of M1, S1BF and V1 on the 3D map were consistent with the results measured using coronal CT images, as shown in Figure 3B, and the distribution pattern of cortical thickness on the 3D maps was the same between *grt/grt* and *grt/+*.

A. Nissl staining (high-magnification images)



B. NeuN immunostaining (high-magnification images)

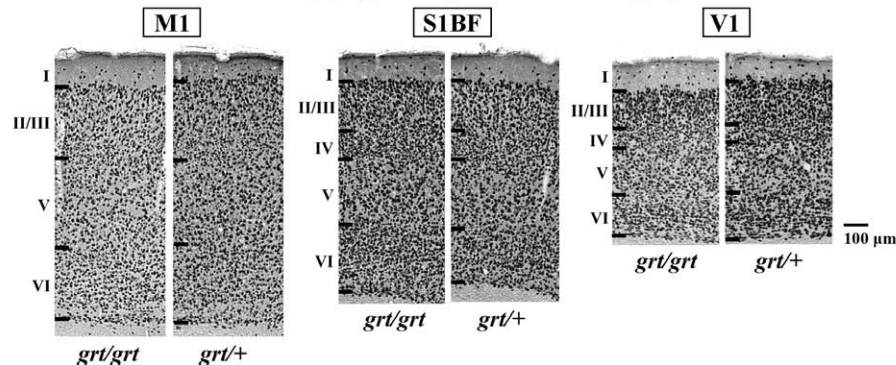


Fig. 4. Cortical histoarchitecture of Nissl staining and NeuN immunostaining. (A) Nissl-stained coronal sections of primary motor (M1), barrel field of primary somatosensory (S1BF) and primary visual (V1) cortices in *grt/grt* and *grt/+*. (B) NeuN-immunostained sections of M1, S1BF and V1 cortices in *grt/grt* and *grt/+*. Layers I–VI were indicated to the left. Layer IV in the M1 was too thin to distinguish in either *grt/grt* or *grt/+*. There was no visible difference in layers (I–VI) between *grt/grt* and *grt/+*.

Next, using Nissl-stained coronal sections, we measured cortical thickness in three cortical areas. Photomicrographs of Nissl staining in three functional cortical areas, including M1, S1, and V1, were shown (Fig. 4A). The thickness of each cortical area was quantified, and the results were shown in Figure 5A. Two-way ANOVA revealed significant effects on cortical areas ($F_{2,24}=218.95$, $P<0.001$), but not on genotypes.

Cortical histoarchitecture

As mentioned in the above sections, cortical thickness in the representative cortical areas was not altered in *grt/grt*. Next, we examined whether or not cerebral abnormalities in *grt/grt* were obtained at histoarchitectural levels. We selected three areas that had different functions and were located vertically to pial surface on coronal sections, i.e., the primary motor cortex (M1), barrel field of primary somatosensory cortex (S1BF)

and primary visual cortex (V1) (measurements were also made of the cortical thickness).

The laminar structure of the cerebral cortex was examined in three cortical areas, i.e., the M1, S1BF and V1, by Nissl-stained and NeuN-immunostained sections. In the S1BF and V1, six layers of the cortex consisting of different types of neurons were defined in both Nissl- and NeuN-immunostained sections (Fig. 4). In the M1, layer IV was unclear and too thin to define (Fig. 4). Consistent with the results measured on coronal CT images, the thickness of all three cortical areas measured using NeuN-immunostained sections were not different between *grt/grt* and *grt/+*. We further measured the thickness of each cortical layer in all three cortical areas using NeuN-immunostained sections, and the results are shown in Figure 5B. Two-way ANOVA revealed no significant effects on cortical layers (layers I, II/III, IV, V and/or VI) or genotypes (*grt/grt* and *grt/+*), or in their interactions in any of the three cortical areas.

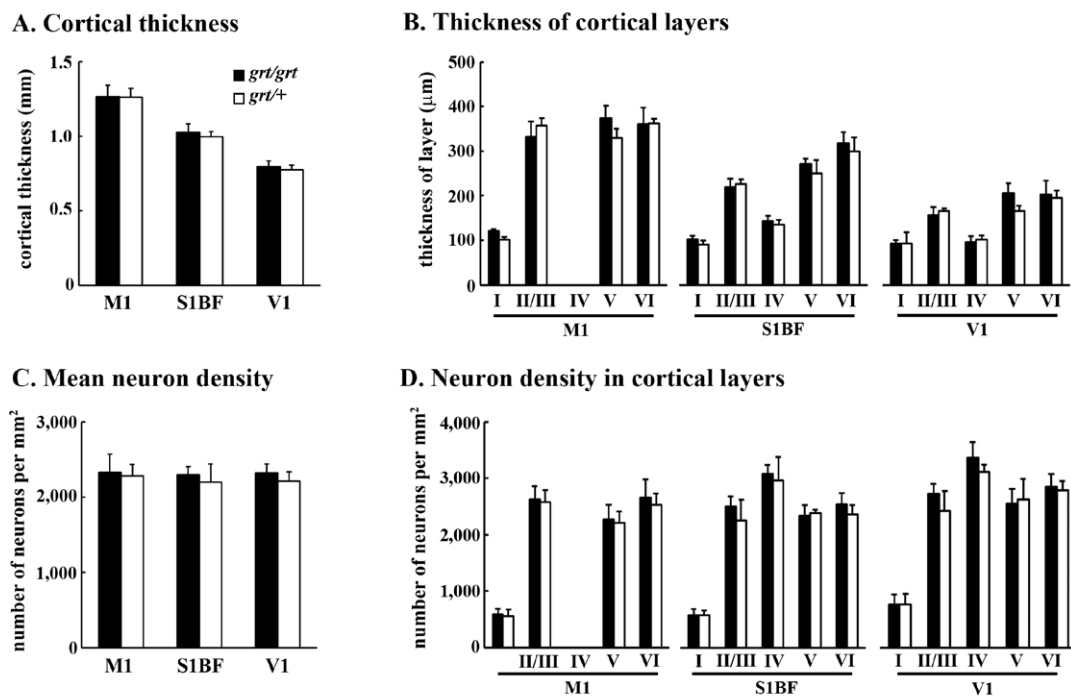


Fig. 5. Bar graphs of thickness and neuron density in cerebral cortex. (A) Bar graphs showing cortical thickness of primary motor (M1), barrel field of primary somatosensory (S1BF) and primary visual (V1) cortex in *grt/grt* and *grt/+*. No significant effect on cortical thickness in three cortical areas between *grt/grt* and *grt/+* was noted by two-way ANOVA. (B) Bar graphs showing thickness of layers I, II/III, IV, V and VI in *grt/grt* and *grt/+*. No significant effect on the thickness of each layer between *grt/grt* and *grt/+* was noted in three cortical areas by two-way ANOVA. (C) Bar graphs showing NeuN-immunoreactive neuron density of M1, S1BF and V1 in *grt/grt* and *grt/+*. No significant effect on neuron density in three cortical areas between *grt/grt* and *grt/+* was noted by two-way ANOVA. (D) Bar graphs showing NeuN immunoreactive neurons of layers I, II/III, IV, V and VI in M1, S1BF and V1 of *grt/grt* and *grt/+*. No significant effect on the neuron density of each layer between *grt/grt* and *grt/+* was noted in three cortical areas by two-way ANOVA.

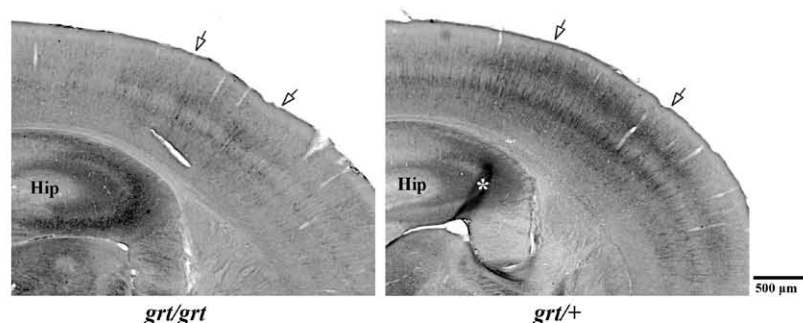
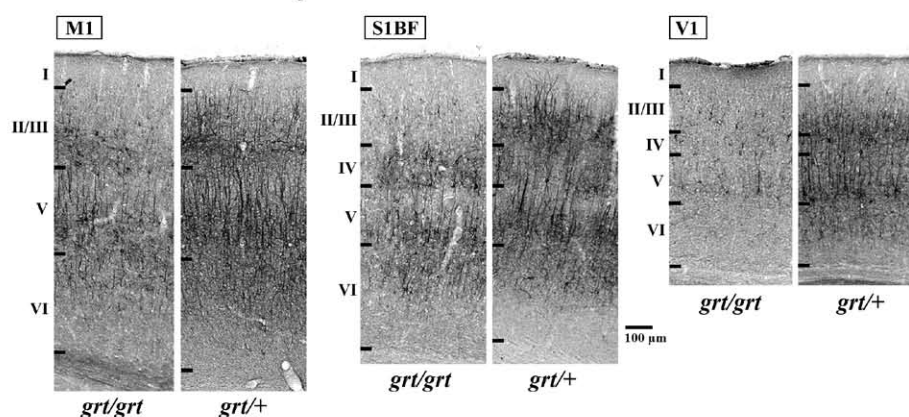
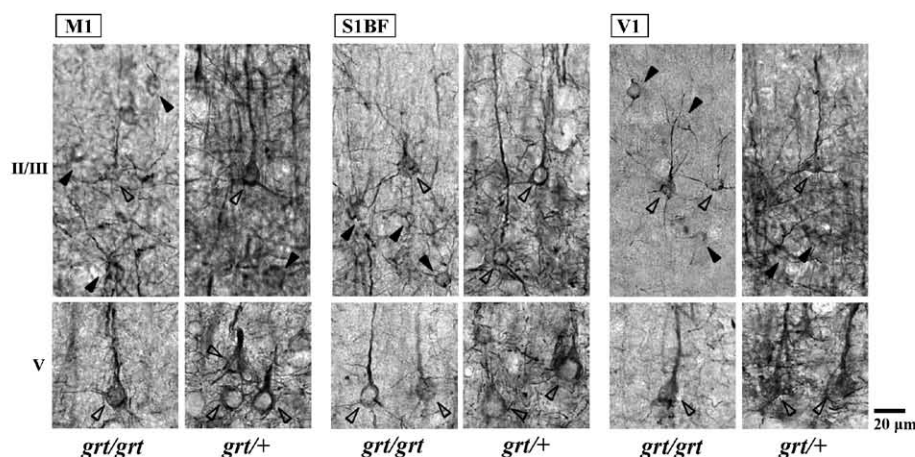
A. SMI-32 immunostaining (low-magnification images)**B. SMI-32 immunostaining of three cortical areas****C. SMI-32 immunostaining (high-magnification images)**

Fig. 6. SMI-32 immunostaining in cerebral cortex. (A) Low-magnification images on coronal sections at the rostral portion of hippocampus in *grt/grt* and *grt/+*. Between arrows, the barrel field of somatosensory cortex (S1BF) is indicated. While two strata of SMI-32 immunostaining were seen in S1BF of both genotypes, staining intensity was attenuated in *grt/grt*. Asterisk indicates an artificial wrinkle of the section. (B) SMI-32 immunostaining of three different cortical areas: the primary motor cortex (M1), S1BF, and primary visual cortex (V1). An overall reduction in SMI-32 immunostaining was observed throughout cortical layers in the M1, S1BF and V1 of *grt/grt*. In particular, the outer half of M1 and S1BF outer strata attenuated neuropil staining. (C) High magnification images of SMI-32 immunostaining. SMI-32 immunostaining appeared in pyramidal neurons (indicated by open arrowheads) and multipolar neurons (closed arrowheads). Pyramidal neurons with pale apical dendrites also exhibited weak SMI-32 immunostaining in the inner stratum. (Hip) hippocampus.

Next, we estimated the density of neurons in the entire depth and in each layer of the cortex using NeuN-immunostained sections (Fig. 5C). The neuron density of the entire depth of the cortex was the same among three cortical areas examined with *grt/grt* and *grt/+* (Fig. 5C). Two-way ANOVA revealed no significant effects on cortical areas and genotypes. The neuron density of each cortical layer was estimated in all three cortical areas examined. While neuron density varied among cortical layers in each cortical area, there was no difference in density between *grt/grt* and *grt/+* (Fig. 5D). Two-way ANOVA was conducted with cortical layers (layers I, II/III, IV, V and/or VI) and genotypes of mice (*grt/grt* and *grt/+*) as factors. There was a significant effect on cortical layers in the M1 ($F_{3,32}=274.2122$, $P<0.001$), S1BF ($F_{4,40}=205.8512$, $P<0.001$), and V1, ($F_{4,40}=79.1106$, $P<0.001$), but not on genotypes or interactions between cortical layers and genotypes.

SMI-32 immunostaining

Anti-SMI-32 is recognized as a non-phosphorylated form of the neurofilament heavy chain that distinguishes distinct populations of mature pyramidal neurons in layers III and V of the neocortex (Van der Gucht et al. 2007). Next, arrangements of pyramidal neurons in the representative cortical areas were examined in *grt/grt* mice. Low-magnification images

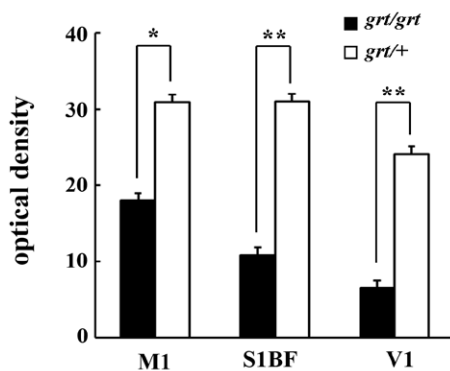


Fig. 7. Semi-quantitative evaluation of SMI-32 staining intensity in cerebral cortex. Bar graphs show the optical density (OD) in the primary motor cortex (M1), barrel field of somatosensory cortex (S1BF) and primary visual cortex (V1). Two-way ANOVA revealed significant effects on genotypes ($F_{1,24}=37.0137$; $P<0.05$) and cortical areas ($F_{2,24}=3.6866$; $P<0.001$), but not on the interaction of the two. * $P<0.05$, ** $P<0.01$ (Scheffé's test).

of SMI-32 immunostaining on coronal sections at the rostral portion of hippocampus in *grt/grt* and *grt/+* are shown in Figure 6A. The dorsolateral region of the cortex in these sections corresponded to the S1BF (between arrows in Fig. 6A) in both *grt/grt* and *grt/+*. Two strata of SMI-32 immunostaining appeared in the S1BF in *grt/+* (Fig. 6A). Such SMI-32 immunopositive strata were also seen in the M1 and V1 (Fig. 6B). Two SMI-32 immunopositive strata in each of the three cortical areas examined were segregated by a negative gap throughout the outer half of layer V: the outer stratum corresponded to layers II/III in the M1 and layers II-IV in the S1BF and V1; the inner stratum corresponded to the inner half of layer V in the M1, S1BF and V1 (Fig. 6B). In high magnification images, SMI-32 immunostaining appeared in pyramidal and multipolar neurons in both the inner and outer strata. High-magnification images revealed an intense SMI-32 immunostaining with apical dendrites of pyramidal neurons and dendritic arbors of multipolar neurons (Fig. 6C). While two types of SMI-32 immunostained dendrites intertwined with each other in a complex manner, SMI-32 immunopositive multipolar neurons were more numerous in the outer than in the inner stratum.

In *grt/grt*, SMI-32 immunostaining in both the outer and inner strata was attenuated in the M1, S1BF and V1 (Fig. 6B). Such reduced immunostaining was specific to the neocortex, because SMI-32 immunostaining was sustained in the hippocampus of *grt/grt* (Fig. 6A). Although an overall reduction in SMI-32 immunostaining was observed throughout the cortical layers in the M1 and S1BF of *grt/grt*, the outer half of the outer strata especially attenuated neuropil staining (Fig. 6B). In both the inner and outer strata, pyramidal neurons with pale and irregularly extended apical dendrites exhibited weak SMI-32 immunostaining (Fig. 6B). Morphology and SMI-32 immunostaining in multipolar neurons were relatively sustained (Fig. 6C).

The most attenuated SMI-32 immunostaining throughout the cortical layers of *grt/grt* was seen in the V1 (Fig. 6B). SMI-32-immunostained pyramidal neurons were seen often in the inner stratum, but not in the outer stratum (Fig. 6B). An extreme reduction in SMI-32 immunostaining in pyramidal neurons resulted in SMI-32 immunopositive multipolar neurons standing out especially, particularly in the outer stratum (Fig. 6B,C).

In order to evaluate the intensity of SMI-32 immunostaining, optical density (OD) was measured in the

M1, S1BF and V1, and compared between *grt/grt* and *grt/+*. Since dendrites of two types of SMI-32 immunoreactive neurons, pyramidal and multipolar, were intertwined with each other, particularly in the region where those dendrites were densely present, we measured OD through the entire depth in each cortical area. As with the visual evaluation, OD in all three cortical areas was lower in *grt/grt* than in *grt/+*, while the lowest OD was marked in the V1 of *grt/grt* (Fig. 7). Two-way ANOVA revealed significant effects on genotypes ($F_{1,24}=37.0137$; $P<0.05$) and cortical areas ($F_{2,24}=3.6866$; $P<0.001$), but not on the interactions of the two. *Post-hoc* testing indicated significantly lower OD in M1, S1, and V1 in *grt/grt* as opposed to *grt/+*. Therefore, reduced SMI-32 immunostaining in the three cortical areas examined was overall, not region-specific.

Thicknesses of corpus callosum

Since reduced volume of cerebral white matter (Fig. 2) and an overall reduction in SMI-32 immunostaining in layer III pyramidal neurons (Figs 6 and 7) were revealed

in *grt/grt*, the thickness of corpus callosum, about 80% of which consists of the callosal fibers derived from layers II/III in rodents (Fame et al. 2011), was compared between *grt/grt* and heterozygous *grt/+*. Thickness of the corpus callosum was examined at the midline of coronal CT images at the center of the anterior commissure (see Fig. 8A,B). The corpus callosum was significantly thinner in *grt/grt* than in *grt/+* ($P<0.05$) (Fig. 7C).

DISCUSSION

The present CT-based volumetry revealed a region-specific reduction of cortical volume in the cerebrum of *grt/grt* mice. The frontooccipital length of the cortex was significantly smaller in *grt/grt* than in heterozygous *grt/+* controls, whereas the cortical widths at the anterior commissure and posterior commissure were not altered in *grt/grt* mice. However, there were no differences in cortical thickness and neuronal density in any of the three cortical areas examined (M1, S1BF and V1) between both genotypes. Those results suggest that cortical hypoplasia in *grt/grt* mice is charac-

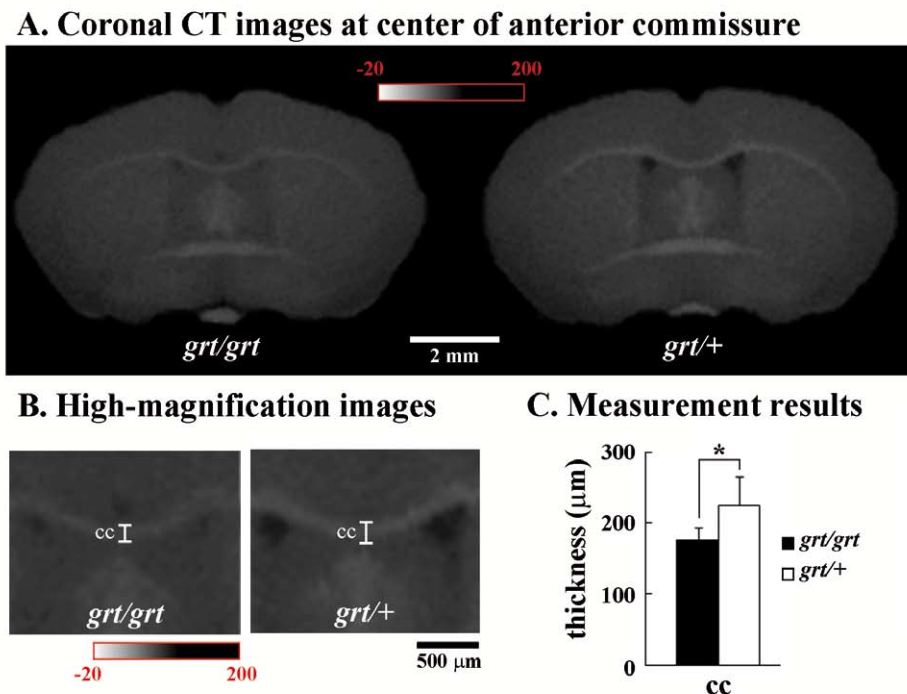


Fig. 8. Thickness of corpus callosum. (A) Coronal CT images at the center of anterior commissure. Thickness of corpus callosum was measured using five serial images including these images, and the mean of five points was used as individual values. The range of Hounsfield units used in CT images is shown enclosed by a red frame. (B) High magnification images of corpus callosum (cc). Measurements were made at the midline in each image. The range of Hounsfield units used in CT images is shown enclosed by a red frame. (C). Measurement of corpus callosum thickness. * $P<0.05$ (Student's *t*-test).

terized by a reduction in the number of cortical neurons at the frontooccipital axis, forming a round-shaped morphology. The present study further examined the laminar organization of the *grt/grt* cortex by SMI-32 immunostaining, which distinguishes distinct populations of mature pyramidal neurons in the neocortex (Van der Gucht et al. 2007). Although SMI-32 immunostaining was seen in both perikarya and apical dendrites of pyramidal neurons in layers III and V of the neocortex of *grt/grt*, SMI-32 immunostaining was attenuated strikingly in pyramidal neurons in layer III of the M1 and S1BF, and layers III and V of the V1 in *grt/grt* mice. Since SMI-32 immunostaining in cortical pyramidal neurons is associated with maturation of those neurons (Kirkcaldie et al. 2002), the present immunohistochemical results suggest the presence of an immature chemical phenotype in the pyramidal neurons of the *grt/grt* cortex. This may be involved in the cortical hypoplasia of *grt/grt* mice.

The present study further revealed a reduced volume of cerebral white matter with thinning of the corpus callosum in the *grt/grt* cerebrum. Callosal projection neurons are present in approximately 80% of layers II/III, and in approximately 20% of layer V in rodents (Fame et al. 2011). Therefore, the immaturity of the chemical phenotype of layer III cortical neurons in *grt/grt* mice may be related to the insufficient development of callosal fibers arising from those neurons.

Tissue-specific expression of the *Tpst2* gene has been reported in the brain (Ouyang and Moore 1998). Tyrosine protein sulfation in the adult rat brain is crucial for the maturation and secretion processes of bioactive cholecystokinin (Dam Trung Tuong et al. 1993), which can induce a long-lasting increase in the excitability of the neocortical network of pyramidal cells (Gallopín et al. 2006). Although the roles of the *Tpst2* gene and/or tyrosine protein sulfation in the brain development are still unclear, the cortical hypoplasia accompanied by immature pyramidal neurons and insufficient development of callosal fibers of *grt/grt* mice in the present study suggest that the *Tpst2* gene defect alters the neocortical network organization arising from pyramidal neurons.

Another possible cause of cortical hypoplasia in *grt/grt* mice is a status caused by the *Tpst2* gene defect, characterized by an elevation of serum/plasma TSH levels (Kobayashi et al. 2001, Sasaki et al. 2007), but with a reduction in serum/plasma thyroxine (T_4) levels (Kobayashi et al. 2001, Yoshida et al. 1994). Since *Tpst2* is crucial for TSH signaling by the tyrosine sul-

fation of TSH receptors (Costagliola et al. 2002), such hypothyroid characteristics of *grt/grt* mice are considered to involve TSH receptor insensitivity (Yoshida et al. 1994, Kobayashi et al. 2001). Congenital hypothyroidism is known to be associated with neurodevelopmental disorders such as cognitive disorder (Dugbartey 1998), dissociating attention deficits (Rovet and Hepworth 2001), autism spectrum disorder (Gillberg et al. 1992), mental retardation, and anxiety (Rastogi and LaFranchi 2010, Grüters and Krude 2011). Those disorders are considered to involve deficiency of thyroid hormones during neurogenesis and/or neuronal development. Notably, experimentally-induced hypothyroid animals have similar characteristics as those of cortical hypoplasia of *grt/grt* mice. Altered morphology of cortical pyramidal neurons has been reported in thyroidectomized rats, with a reduced number of pyramidal cell spines in the visual cortex (Ruiz-Marcos et al. 1979) and a decreased size of layer V pyramidal neurons (Berbel et al. 1993). Myelinated axons in the corpus callosum were greatly reduced in number in hypothyroid rats by the induction of prenatal methimazole treatments followed by neonatal thyroidectomy (Berbel et al. 1994). Therefore, further study will be needed to ascertain whether thyroid hormone administration can improve the cortical hypoplasia of *grt/grt* mice.

CONCLUSION

The present CT-based volumetry combined with semi-quantitative immunohistochemistry suggests that cerebral abnormalities in *grt/grt* mice are characterized by cortical hypoplasia at the frontooccipital axis with immature pyramidal neurons and insufficient development of callosal fibers. In our recent study, a dose-related reduction of cerebellar cortical volumes in rats from prenatal X-irradiation was revealed by MRI-based volumetry (Sawada et al. 2013). Thus, volumetric analysis using CT and MRI can screen the region-specific changes in brain structures in small laboratory animal models. This approach is advantageous, particularly for screening changes in brain structures before destructive approaches such as histological, biochemical and molecular biological analyses.

ACKNOWLEDGEMENT

This study was supported by a grant from Tsukuba International University.

REFERENCES

- Acosta MT, Munasinghe J, Pearl PL, Gupta M, Finegersh A, Gibson KM, Theodore WH (2010) Cerebellar atrophy in human and murine succinic semialdehyde dehydrogenase deficiency. *J Child Neurol* 25: 1457–1461.
- Agui T, Miyamoto T, Tsumura H, Yoshida T (1997) Mapping on the *grt* locus to mouse Chromosome 5. *Mamm Genome* 8: 944.
- Bath KG, Jing DQ, Dincheva I, Neeb CC, Pattwell SS, Chao MV, Lee FS, Ninan I (2012) BDNF Val66Met impairs fluoxetine-induced enhancement of adult hippocampus plasticity. *Neuropsychopharmacology* 37: 1297–1304.
- Berbel P, Guadaño-Ferraz A, Martínez M, Quiles JA, Balboa R, Innocenti GM (1993) Organization of auditory callosal connections in hypothyroid adult rats. *Eur J Neurosci* 5: 1465–1478.
- Berbel P, Guadaño-Ferraz A, Angulo A, Ramón Cerezo J (1994) Role of thyroid hormones in the maturation of interhemispheric connections in rats. *Behav Brain Res* 64: 9–14.
- Bigler ED, Abildskov TJ, Petrie JA, Johnson M, Lange N, Chipman J, Lu J, McMahon W, Lainhart JE (2010) Volumetric and voxel-based morphometry findings in autism subjects with and without macrocephaly. *Dev Neuropsychol* 35: 278–295.
- Costagliola S, Panneels V, Bonomi M, Koch J, Many MC, Smits G, Vassart G (2002) Tyrosine sulfation is required for agonist recognition by glycoprotein hormone receptors. *EMBO J* 21: 504–513.
- Dam Trung Tuong M, Vargas F, Brion F, Frerot O (1993) Subcellular and developmental studies of the tyrosyl protein sulfotransferase in rat brain. *Int J Biochem* 25: 713–718.
- Dorr AE, Lerch JP, Spring S, Kabani N, Henkelman RM (2008) High resolution three-dimensional brain atlas using an average magnetic resonance image of 40 adult C57Bl/6J mice. *Neuroimage* 42: 60–69.
- Dugbartey AT (1998) Neurocognitive aspects of hypothyroidism. *Arch Intern Med* 158: 1413–1418.
- Fame RM, MacDonald JL, Macklis JD (2011) Development, specification, and diversity of callosal projection neurons. *Trends Neurosci* 34: 41–50.
- Gallopín T, Geoffroy H, Rossier J, Lambolez B (2006) Cortical sources of CRF, NKB, and CCK and their effects on pyramidal cells in the neocortex. *Cereb Cortex* 16: 1440–1452.
- Gillberg IC, Gillberg C, Kopp S (1992) Hypothyroidism and autism spectrum disorders. *J Child Psychol Psychiatry* 33: 531–542.
- Grüters A, Krude H (2011) Detection and treatment of congenital hypothyroidism. *Nat Rev Endocrinol* 8: 104–113.
- Heikkinen T, Lehtimäki K, Vartiainen N, Puoliväli J, Hendricks SJ, Glaser JR, Bradaia A, Wadel K, Touller C, Kontkanen O, Yrjänheikki JM, Buisson B, Howland D, Beaumont V, Munoz-Sanjuan I, Park LC (2012) Characterization of neurophysiological and behavioral changes, MRI brain volumetry and 1H MRS in zQ175 knock-in mouse model of Huntington's disease. *PLoS One* 7: e50717.
- Horiuchi-Hirose M, Sawada K, Fukui Y (2012) Laminar cytoarchitecture of cerebral cortex in Ca_v2.1 mutant, rolling mouse Nagoya. *Curr Neurobiol* 3: 85–89.
- Howard RJ, Almeida O, Levy R, Graves P, Graves M (1994) Quantitative magnetic resonance imaging volumetry distinguishes delusional disorder from late-onset schizophrenia. *Br J Psychiatry* 165: 474–480.
- Huang H, Xue R, Zhang J, Ren T, Richards LJ, Yarowsky P, Miller MI, Mori S (2009) Anatomical characterization of human fetal brain development with diffusion tensor magnetic resonance imaging. *J Neurosci* 29: 4263–4273.
- Iwashiro N, Suga M, Takano Y, Inoue H, Natsubori T, Satomura Y, Koike S, Yahata N, Murakami M, Katsura M, Gonoï W, Sasaki H, Takao H, Abe O, Kasai K, Yamasue H (2012) Localized gray matter volume reductions in the pars triangularis of the inferior frontal gyrus in individuals at clinical high-risk for psychosis and first episode for schizophrenia. *Schizophr Res* 137: 124–131.
- Joyal CC, Pennanen C, Tiihonen E, Laakso MP, Tiihonen J, Aronen HJ (2004) MRI volumetry of the vermis and the cerebellar hemispheres in men with schizophrenia. *Psychiatry Res* 131: 115–124.
- Kirkcaldie MT, Dickson TC, King CE, Grasby D, Riederer BM, Vickers JC (2002) Neurofilament triplet proteins are restricted to a subset of neurons in the rat neocortex. *J Chem Neuroanat* 24: 163–171.
- Kobayashi K, Yamamoto H, Kobayashi T, Machida T (2001) Responses of the thyroid gland to TSH and other thyroid stimulators in growth-retarded (*grt*) mouse. *Zool Sci* 18: 955–961.
- Molina V, Sanz J, Sarraimea F, Luque R, Benito C, Palomo T (2006) Dorsolateral prefrontal and superior temporal volume deficits in first-episode psychoses that evolve into schizophrenia. *Eur Arch Psychiatry Clin Neurosci* 256: 106–111.
- Ouyang YB, Moore KL (1998) Molecular cloning and expression of human and mouse tyrosylprotein sulfotransferase-2 and a tyrosylprotein sulfotransferase homo-

- logue in *Caenorhabditis elegans*. *J Biol Chem* 273: 24770–24774.
- Paxinos G, Franklin KBJ (2004) *The Mouse Brain in Stereotaxic Coordinates* (2nd edition). Elsevier Academic Press, San Diego, CA.
- Preuss UW, Zetzsche T, Pogarell O, Mulert C, Frodl T, Müller D, Schmidt G, Born C, Reiser M, Möller HJ, Hegerl U, Meisenzahl EM (2010) Anterior cingulum volumetry, auditory P300 in schizophrenia with negative symptoms. *Psychiatry Res* 183: 133–139.
- Rastogi MV, LaFranchi SH (2010) Congenital hypothyroidism. *Orphanet J Rare Dis* 5: 17.
- Rovet JF, Hepworth SL (2001) Dissociating attention deficits in children with ADHD and congenital hypothyroidism using multiple CPTs. *J Child Psychol Psychiatry* 42: 1049–1056.
- Ruiz-Marcos A, Sanchez-Toscano F, Escobar del Rey F, Morreale de Escobar G (1979) Severe hypothyroidism and the maturation of the rat cerebral cortex. *Brain Res* 162: 315–329.
- Saito S, Murase K (2012) Ex vivo imaging of mouse brain using micro-CT with non-ionic iodinated contrast agent: a comparison with myelin staining. *Br J Radiol* 85: e973–978.
- Sasaki N, Hosoda Y, Nagata A, Ding M, Cheng JM, Miyamoto Y, Okano S, Asano A, Miyoshi I, Agui T (2007) A mutation in *tpst2* encoding tyrosylprotein sulfotransferase causes dwarfism associated with hypothyroidism. *Mol Endocrinol* 21: 1713–1721.
- Sawada K, Hosoi E, Bando M, Sakata-Haga H, Lee NS, Jeong YG, Fukui Y (2008) Differential alterations in expressions of ryanodine receptor subtypes in cerebellar cortical neurons of an ataxic mutant, rolling mouse Nagoya. *Neuroscience* 152: 609–617.
- Sawada K, Saito S, Horiuchi-Hirose M, Mori Y, Yoshioka Y, Murase K (2013) Dose-related cerebellar abnormality in rats with prenatal exposure to X-irradiation by MRI volumetric analysis. *Congenit Anom (Kyoto)* 53: 127–130.
- Sawiak SJ, Wood NI, Williams GB, Morton AJ, Carpenter TA (2009) Use of magnetic resonance imaging for anatomical phenotyping of the R6/2 mouse model of Huntington's disease. *Neurobiol Dis* 33: 12–19.
- Saze T, Hirao K, Namiki C, Fukuyama H, Hayashi T, Murai T (2007) Insular volume reduction in schizophrenia. *Eur Arch Psychiatry Clin Neurosci* 257: 473–479.
- Scheenstra A, Dijkstra J, van der Weerd L (2011) Volumetry and other quantitative measurements to assess the rodent brain. *Methods Mol Biol* 771: 277–291.
- Sun J, Maller JJ, Guo L, Fitzgerald PB (2009) Superior temporal gyrus volume change in schizophrenia: a review on region of interest volumetric studies. *Brain Res Rev* 61: 14–32.
- Van der Gucht E, Hof PR, Van Brussel L, Burnat K, Arckens L (2007) Neurofilament protein and neuronal activity markers define regional architectonic parcellation in the mouse visual cortex. *Cereb Cortex* 17: 2805–2819.
- Verma S, Sitoh YY, Ho YC, Poon LY, Subramaniam M, Chan YH, Sim K, Chong SA (2009) Hippocampal volumes in first-episode psychosis. *J Neuropsychiatry Clin Neurosci* 21: 24–29.
- Whitworth AB, Kemmler G, Honeder M, Kremser C, Felber S, Hausmann A, Walch T, Wanko C, Weiss EM, Stuppaeck CH, Fleischhacker WW (2005) Longitudinal volumetric MRI study in first- and multiple-episode male schizophrenia patients. *Psychiatry Res* 140: 225–237.
- Yoshida Y, Yamanaka K, Atsumi S, Tsumura H, Sasaki R, Tomita K, Ishikawa E, Ozawa H, Watanabe K, Totsuka T (1994) A novel hypothyroid 'growth-retarded' mouse derived from Snell's dwarf mouse. *J Endocrinol* 142: 435–446.
- Zeegers M, Hulshoff Pol H, Durston S, Nederveen H, Schnack H, Van Daalen E, Dietz C, Van Engeland H, Buitelaar J (2009) No differences in MR-based volumetry between 2- and 7-year-old children with autism spectrum disorder and developmental delay. *Brain Dev* 31: 725–730.
- Zhang J, Richards LJ, Yarowsky P, Huang H, van Zijl PC, Mori S (2003) Three-dimensional anatomical characterization of the developing mouse brain by diffusion tensor microimaging. *Neuroimage* 20: 1639–1648.